Electrochimica Acta 180 (2015) 1014–1022

Contents lists available at ScienceDirect

Electrochimica Acta

journal homepage: www.elsevier.com/locate/electacta

Hybridization of Graphene in 3D Complex Nanovoids: Synergistic Nanocomposites for Electrocatalytic Reduction of Hydrogen Peroxide

Wen-Jie Lan, Chun-Hu Chen*

Department of Chemistry, National Sun Yat-sen University, Kaohsiung, Taiwan 80424

ARTICLE INFO

Article history:
Received 21 July 2015
Received in revised form 10 August 2015
Accepted 7 September 2015
Available online 9 September 2015

Keywords:
graphene
nanostructures
hydrogen peroxide
sensors
synergistic electrocatalysis

ABSTRACT

Graphene hybrids comprised of diverse functional materials have shown exceptional performance. However, only 2D composites were widely studied, the understanding of graphene hybridization behavior with complex 3D nanostructures remains unclear. In this work, we investigate how the graphene hybridization is affected by the presence of 3D nanovoids, and the corresponding influence on the electrocatalysis of hydrogen peroxide reduction. The 3D nanovoids of the cobalt manganese oxide (CMO) increase the amount of graphene captured in the composites for the higher surface areas, uniform porosity, and improved electrocatalytic activities. The formation of graphene/CMO interfaces contributes to the efficient H_2O_2 reduction at the more positive onset potentials than graphene or CMO material alone. Controls of the inhomogeneous distribution and void-filling behavior of graphene on CMO surface are critical to achieve optimal, synergistic electrocatalysis. The graphene/CMO hybrids with full graphene coverage exhibit the greatly enhanced H_2O_2 sensitivity by 2900 and 48 times greater than commercial products and bare CMO, respectively.

1. Introduction

Hybridization of graphene with various functional materials enables these nanocomposites to exhibit exceptional performance [1–6]. The most common methods to produce graphene hybrids are to react graphene colloids with material precursors directly to yield two-dimensional (2D) composites [7–11]. However, 2D nature of the resultants usually suffers from aggregation and stacking issues, causing the difficulty of using these nanocomposites in applications that require highly efficient mass transport and diffusion (e.g. heterogeneous catalysis, sensors, etc.). Expanded internal spacing created by 3D complex nanostructures is advantageous to address these issues [12–15]. Although 3D graphene nanocomposites are desired, the dimensional difference between 3D complex nanostructures and 2D graphene sheets may arise the synthetic challenges to achieve their homogeneous hybridization at the interfaces. Furthermore, the detailed hybridization behaviors of graphene with 3D complex nanostructures, which could greatly influence the properties of the composites, still remain unclear.

Owing to the strong oxidative activity of hydrogen peroxide, catalytic reduction and detection of hydrogen peroxide are critical to address issues of bimolecular damage (e.g. DNA) and surface corrosion of materials [16–19]. Imbalanced hydrogen peroxide in physiological systems involves the onset of cancers, diabetes, and other diseases [20,21]. Recently, release of H_2O_2 through particular enzymatic reaction becomes a general strategy to monitor biologic mechanisms and pathways of specific metabolite or biomolecules [22,23]. Low-cost, robust, and noble metal-free electrocatalysts are required to fulfill the huge demand for electrochemical sensors of hydrogen peroxide. In our previous study, cobalt manganese oxides (CMO) with the tunable nanostructures serve as the proper substrates to study how graphene interacts with 3D nanovoids, and the corresponding changes of the electrocatalytic activities [24]. In addition, CMO with the improved conductivity and mixed valency is advantageous to perform highly sensitive H_2O_2 detection as low-cost and noble metal-free sensors. Successful hybridization of graphene with the nanostructured CMO is expected to significantly enhance the sensing performance.

In this work, we report the hybridization behavior of graphene with the 3D nanovids in cobalt manganese oxide (CMO) for the synergistic electrocatalysis of hydrogen peroxide reduction. The presence of 3D nanovoids traps the greater amount of graphene in the composites, leading to the increase of surface areas, uniform porosity, and the enhanced H_2O_2 sensitivity by 2900 and 48 times higher than commercial cobalt oxides and bare CMO, respectively. The effective interfaces between graphene and CMO are recognized as the new, high-performance electrocatalytic sites. The inhomogeneous distribution of graphene in 3D nanovoids

* Corresponding author. Tel.: +88675252000

http://dx.doi.org/10.1016/j.electacta.2015.09.041
0013-4686/

emphasizes the essential role of continuous charge transport routes to achieve the synergistic performance.

2. Experimental

2.1. Preparation of Cobalt Manganese Oxide (CMO)

To synthesize CMO, deionized (D.I.) water was mixed with $CoSO_4 \cdot 7H_2O$ (8.08 mmol) and $KMnO_4$ (2.69 mmol) to form a purple solution (71 mL) and then transferred to a Teflon-lined autoclave for hydrothermal treatment at 100 °C. The products were calcined in air at 500 °C for 6 hours to yield CMO materials. The smooth surface CMO was prepared hydrothermally at 60 °C.

2.2. Preparation of graphene oxide (GO) colloids

Thin graphene oxide sheets were synthesized from bulk graphite crystals according to the modified Hummers method [25]. Graphite powder (1.0 g), sodium nitrate (0.5 g), and sulfuric acid (100 mL, 96%) were mixed first for 30 min, and then potassium permanganate (6.0 g) was added into the mixture slowly under ice bath. After the removal of ice bath, the reaction temperature was brought to 50 °C for 16 hours. D.I. water (200 mL) and 23 mL of hydrogen peroxide were added into the suspension to reduce the residual permanganate and manganese oxide. The suspension was filtered and washed with HCl (500 mL, 10%) and D.I. water to pH 6. The GO colloidal solutions were further exfoliated by ultrasonication for 30 min, followed by a centrifugation at 14,000 rpm for 10 min to collect the GO sheet suspension (0.2 mg mL^{-1}). The as-obtained GO samples carry negatively charged surface in the range of pH 2–14 [26].

2.3. Preparation of graphene/CMO composites

CMO powder (0.4 g) was first dispersed in 200 mL ethanol by sonication for 30 min, followed by an addition of 2 mL of (3-aminopropyl)-trimethoxysilane (APTMS) for a reflux at 80 °C [27–29]. The as-obtained powder was sufficiently rinsed with ethanol to wash away any remaining APTMS moiety to obtain the APTMS-treated CMO. Different amounts (10, 20, and 40 mg) of the as-prepared GO sheets were added into the APTMS-CMO suspension and refluxed at 100 °C for 24 hours to yield the black powder of GO-CMO hybrids. To reduce the GO into rGO, these GO-CMO hybrids were hydrothermally treated at 180 °C for one hour to produce rGO-CMO hybrids. The rGO-CMO composites prepared with 40, 20, and 10 mg of GO were denoted as **G-CMO**, **G-0.5-CMO**, and **G-0.25-CMO**, respectively. For the preparation of graphene hybrids by direct one-step method, cobalt sulfate (8.08 mmol), potassium permanganate (2.69 mmol), and GO (40 mg) were mixed together in D.I. water of 70 mL to yield a brownish-purple solution and then hydrothermally treated at 100 °C for 24 hours. The precipitates were washed with D.I. water and then dried at 60 °C for 12 hours. Following the suggestion of a reviewer, an additional sample with 90 mg of GO hybridizing with CMO was prepared and tested to understand the effect of thick graphene coating on CMO.

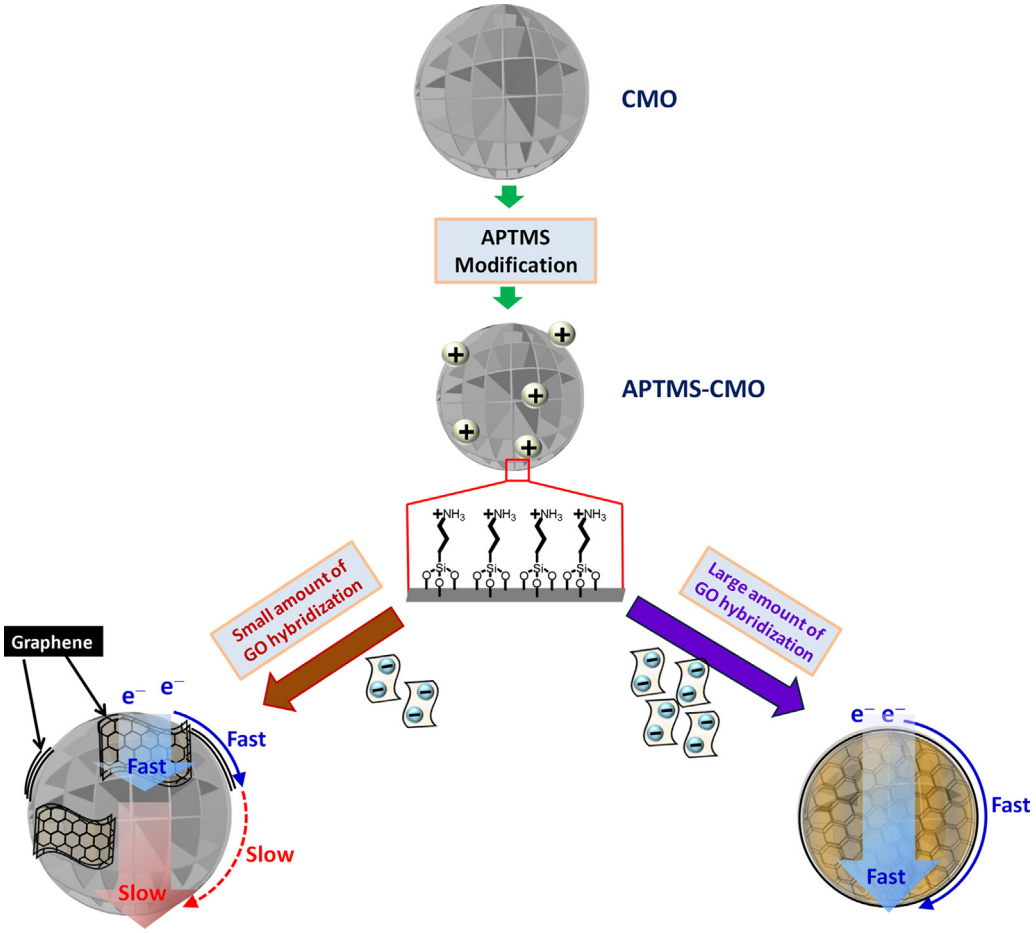

Scheme 1. The illustration of graphene hybridization with complex nanostructures. The APTMS treatment generates the positive charged surface on CMO. The fully graphene-covered CMO composites (e.g. **G-CMO**) exhibits fast charge transportation for electrocatalysis (the right pathway), while the partially graphene-covered CMO with the discontinuous graphene shell suffer from the retarded migration of charges (the left pathway).

2.4. Preparation of G-CMO modified electrodes

A glassy carbon electrode (GCE) with a diameter of 3 mm was polished by alumina slurry to clean the electrode surface first. Various hybrids were ultrasonicated in ethanol (1 mL) for 30 min to obtain a homogeneous suspension. Then 10 μL of the suspension was loaded on a glassy carbon electrode and dried at room temperature. A drop of Nafion (0.1%, 10 μL) was deposited on the top of the dried samples to obtain the modified electrodes for electrochemical measurements.

2.5. Material characterization and electrochemical measurement

The SEM images were acquired using a Zeiss Supra 55 Gemini FE-SEM with a Schottky emitter operating at 5 kV. Transmission electron microscopy (TEM) images were obtained with a FEI Tecnai F20 at 200 kV. Thermogravimetry analysis (TGA) was performed by heating the samples in O_2 with a flow rate of 30 mL min^{-1} on a PerkinElmer TGA4000 thermal analyzer (heating rate: 10 °C min^{-1}). The XRD patterns were acquired using a Bruker D2 Phaser diffractometer with a Cu-Kα X–ray source

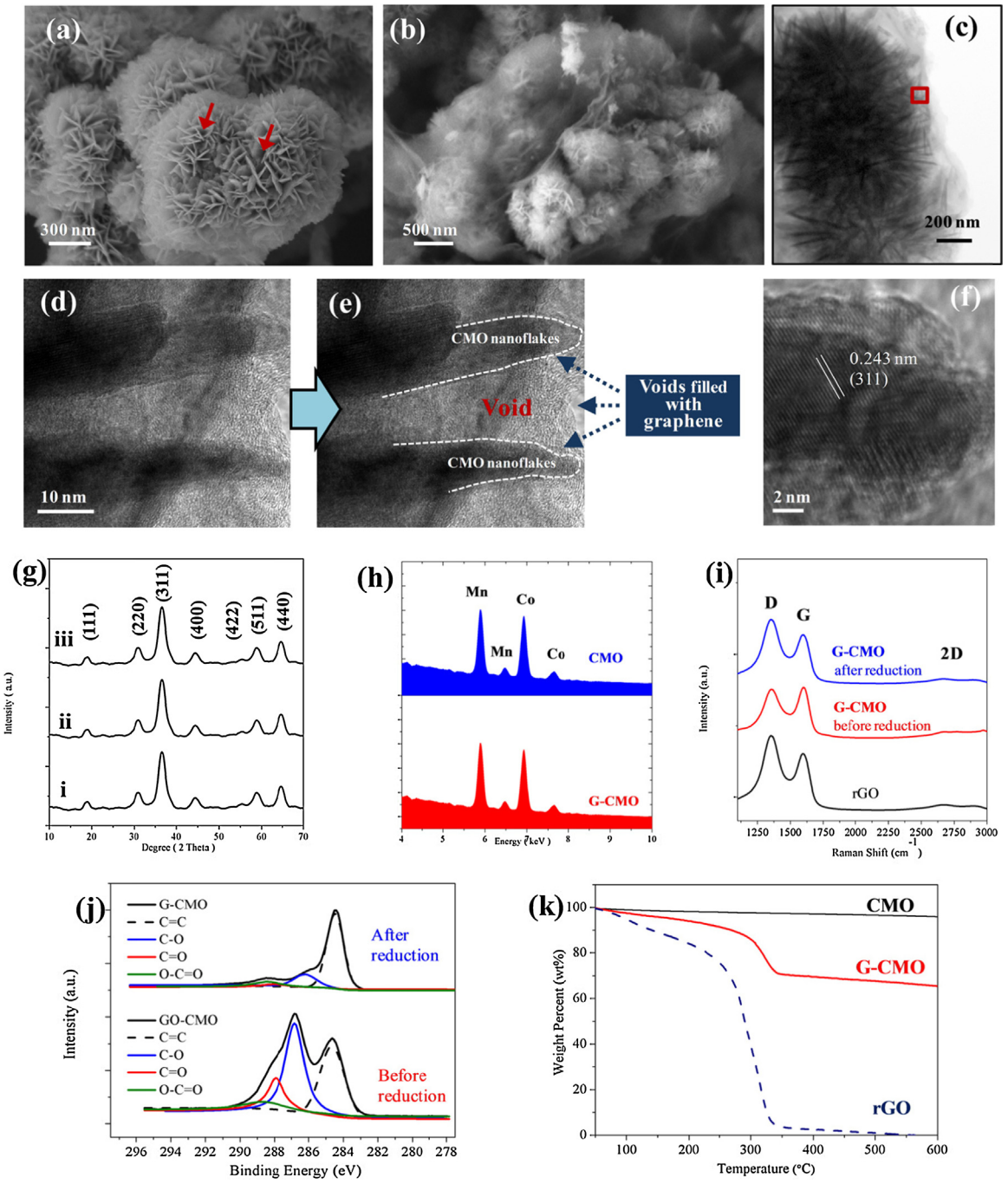

Fig. 1. Graphene–cobalt manganese oxide hybrid materials. (a) The SEM images of bare CMO with the nanostructured voids (red arrows) on the surface. (b) SEM images of **G-CMO**. (c) The TEM images of **G-CMO** with the graphene sheets wrapping on the surface. (d) The higher magnification images correspond to the red square in (c). (e) The marks of nanoflakes (white dash-line) and voids corresponding to the image in (d), presenting the nanostructure voids filled up with graphene (blue arrows). (f) The HR-TEM images of a single flake of **G-CMO**. (g) The XRD patterns of (i) CMO, (ii) APTMS-treated CMO, and (iii) **G-CMO**. (h) The EDXS analysis of CMO and **G-CMO**. (i) The Raman spectra of rGO and **G-CMO**, (j) The XPS results of C 1 s in **G-CMO** before and after hydrothermal reduction. Four different carbon species with the corresponding binding energy (BE), including C=C (284.7 eV), C—O (285.9 eV), C=O (287.6 eV), and O—C=O (289.1 eV) were applied to analyze the spectra. (k) The comparison of TGA profiles of CMO, **G-CMO**, and rGO.

Table 1
The summary of conductivity, surface areas, and graphene content of G-CMO samples.

Sample	Conductivity (S cm^{-1})	Surface area (m^2 g^{-1})	Graphene content (%)
CMO	1.5×10^{-2}	57	–[a]
G-0.25-CMO	2.1×10^{-1}	83	3.60
G-0.5-CMO	4.5×10^{-1}	104	7.13
G-CMO	7.3×10^{-1}	200	15.8

[a] Not available

(λ = 1.5418 Å). Raman spectra were collected on WITec Confocal Raman Microscope Alpha300R with 532 nm laser. The BET surface area and nitrogen adsorption-desorption isotherms were determined using a Micromeritics ASPS 2010 system. The XPS experiments were carried out with a Kratos Axis Ultra DLD with Mg/Al achromatic source. The resistance measurements were conducted with Quatek 5601Y Sheet Resistivity Meter Four Point Probe.

Electrochemical measurement by cyclic voltammograms was recorded at potentials ranged from −1.0 V to 0 V with a scan rate of 50 mV s^{-1} in a 1 mM H_2O_2. Chronoamperograms were carried out with the injection of a certain volume of H_2O_2 solution into a 0.1 M phosphate buffer solution (PBS) at pH = 7.2. Electrochemical measurements were conducted with a conventional three-electrode configuration using Ag/AgCl (saturate NaCl) as the reference electrode and Pt as the counter electrode in a CHI614D electrochemical analyzer.

3. Results and Discussion

3.1. G-CMO preparation and characterization

The hybridization of graphene sheets and nanostructured CMO materials was accomplished by electrostatic attraction between negatively charged colloidal graphene oxide (GO) nanosheets and positively charged surface of CMO. We prepared CMO samples first by the redox reaction of cobalt sulfate and potassium permanganate hydrothermally and followed by the calcination at 500 °C subsequently. The as-obtained CMO was subjected to the surface modification procedure with (3-aminopropyl)-trimethoxysilane (APTMS) to generate positively charged surface [27–29]. GO colloids were refluxed with the APTMS-treated CMO for graphene hybridization, and then hydrothermally treated at 180 °C to convert the hybridized GO into the reduced form, yielding the reduced GO/CMO composites, denoted as **G-CMO**. Compared to GO, the relatively high charge transport and conductivities of rGO are desired to enable stronger electrochemical activity in **G-CMO** [30]. The presence of hydroxyl and carboxyl groups in GO could potentially interfere with the charge transport and thus inhibit electrochemical activities. The synthetic procedure of graphene/CMO hybrids is illustrated in Scheme 1.

Bare CMO shows the 3D hierarchical nanostructures, comprised of nanoflake interconnection with voids surrounded by individual nanoflakes (labeled by red arrows in Fig. 1a) [31]. After graphene hybridization, **G-CMO** was fully wrapped by rGO sheets without a significant change of the original 3D nanostructures in the bare CMO (Fig. 1b). The transmission electron microscopy (TEM) results of **G-CMO** show that the semi-transparent graphene sheets continuously attached on the whole surface of CMO spheres (Fig. 1c). In the higher magnification images of graphene/CMO interface (Fig. 1d), the nanostructured voids located between the nanoflakes (labeled by white dashed lines) were completely filled with graphene, schematically presented in Fig. 1e with the aid of

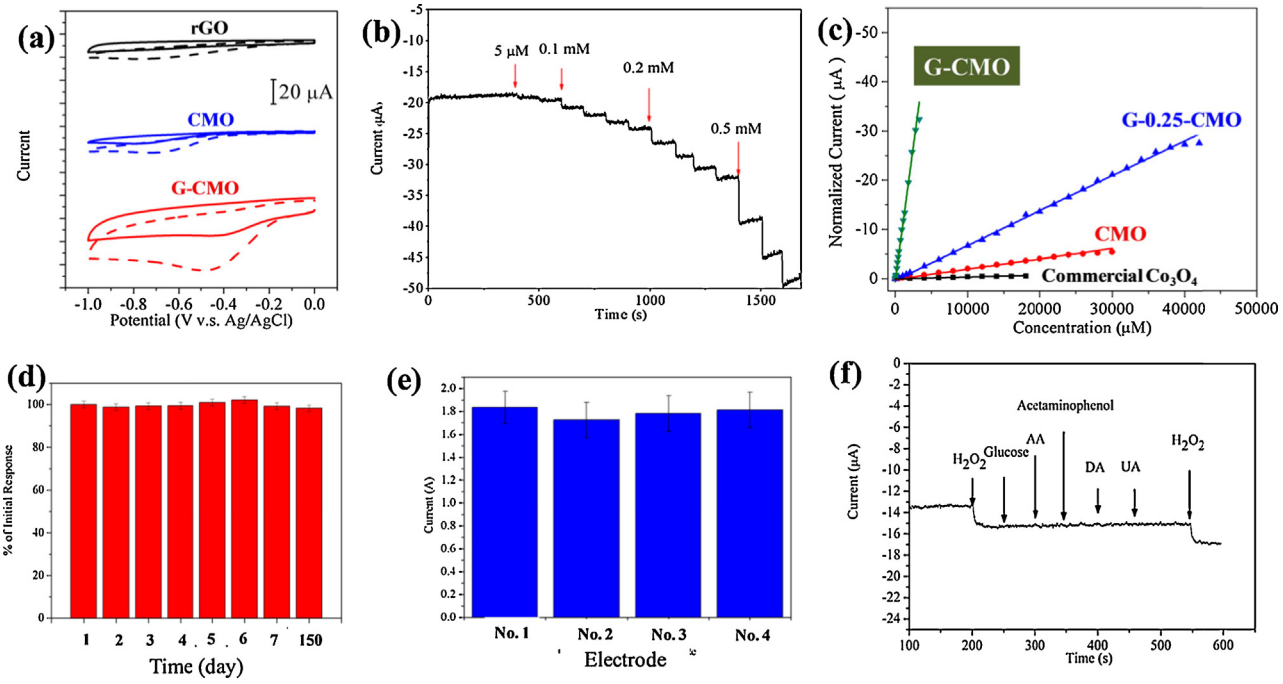

Fig. 2. Graphene–cobalt manganese oxide hybrid as hydrogen peroxide sensors. (a) CV curves of rGO, CMO, and **G-CMO** acquired in blank buffer solutions (solid line) and 1 mM H_2O_2 buffer solutions (dashed line). (b) The amperometric response of **G-CMO** at −0.5 V with successive additions of H_2O_2. (c) The corresponding calibration curves of **G-CMO**,**G-0.25-CMO**, CMO, and commercial Co_3O_4 for the comparison of sensitivities. (d) The continuous tests of H_2O_2 sensing up to 150 days. (e) The comparison of amperometric responses of four different electrodes modified with **G-CMO**. (f) The selectivity studies of **G-CMO** in the presence of interfering species of DA, UA, AA, glucose, and acetaminophen.

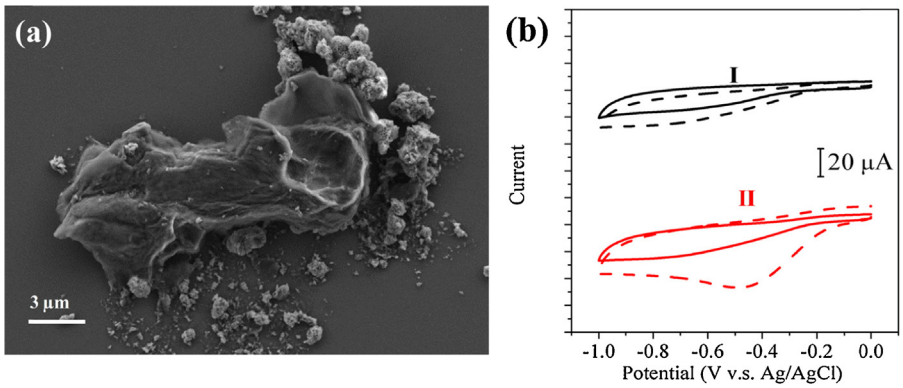

Fig. 3. (a) The SEM images of the product prepared without APTMS modification on CMO surface, showing no interfacial hybridization between graphene stacks and CMO. (b) The CV comparison of the composite in (a), labeled by I, and **G-CMO**, labeled by II, in blank buffer solutions (solid line) and 1 mM H_2O_2 buffer solutions (dashed line).

blue arrows. The high-resolution (HR) TEM images show a lattice spacing of 0.243 nm in CMO nanoflakes, corresponding to the (311) plane of spinel Co_3O_4 structure (Fig. 1f). We observed a complete hybridization of graphene sheets on CMO without the presence of free graphene and nanostructured CMO under TEM. The XRD patterns of CMO samples correspond to spinel Co_3O_4 phase (JCPDS 9-418) before graphene hybridization (Fig. 1g). After APTMS functionalization and GO reduction at 180 °C, the Co_3O_4 phase in CMO remained unchanged. Fig. 1h shows the elemental compositions of bare CMO and **G-CMO**. No significant variation of Co/Mn ratios in **G-CMO** was observed, demonstrating the effective preservation of the intrinsic morphologies/properties of CMO during the hybridization process.

The Raman results of **G-CMO** demonstrate characteristic D and G bands (at ~1355 and 1591 cm^{-1} respectively) that observed in GO and rGO [32], confirming the presence of graphene in **G-CMO** (Fig. 1i). We further acquired the XPS spectra of C1s to identify the generation of rGO (Fig. 1j). The graphene hybrids before hydrothermal treatment show relatively higher contents of oxidized carbon species [33,34], while the significantly lowered levels of that in **G-CMO** were observed after the reduction. CMO samples exhibit the high thermal stability with a weight loss of 3.2% up to 600 °C, while rGO shows a full decomposition at ~300 °C (Fig. 1k). The TGA profiles of **G-CMO** demonstrate a weight loss of 15.8% at 300 °C, identified as the graphene decomposition by referencing the profile of rGO.

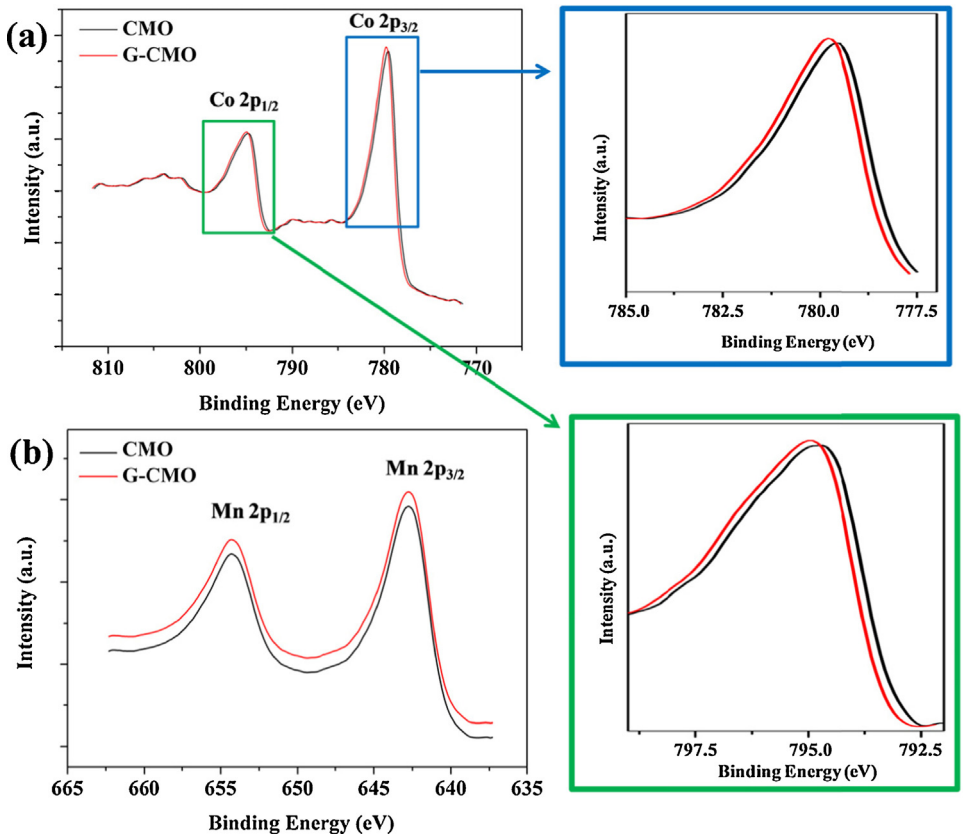

Fig. 4. The XPS comparison of CMO and **G-CMO**. (a) The Co 2p spectra of **G-CMO** exhibit the peak shift to the higher binding energy values as shown in the zoom-in spectra of $2P_{3/2}$ (blue square) and $2P_{1/2}$ (green square), respectively. No appreciable shift was observed for Mn 2p spectra in (b). (For interpretation of the references to color in this figure legend, the reader is referred to the web version of this article.)

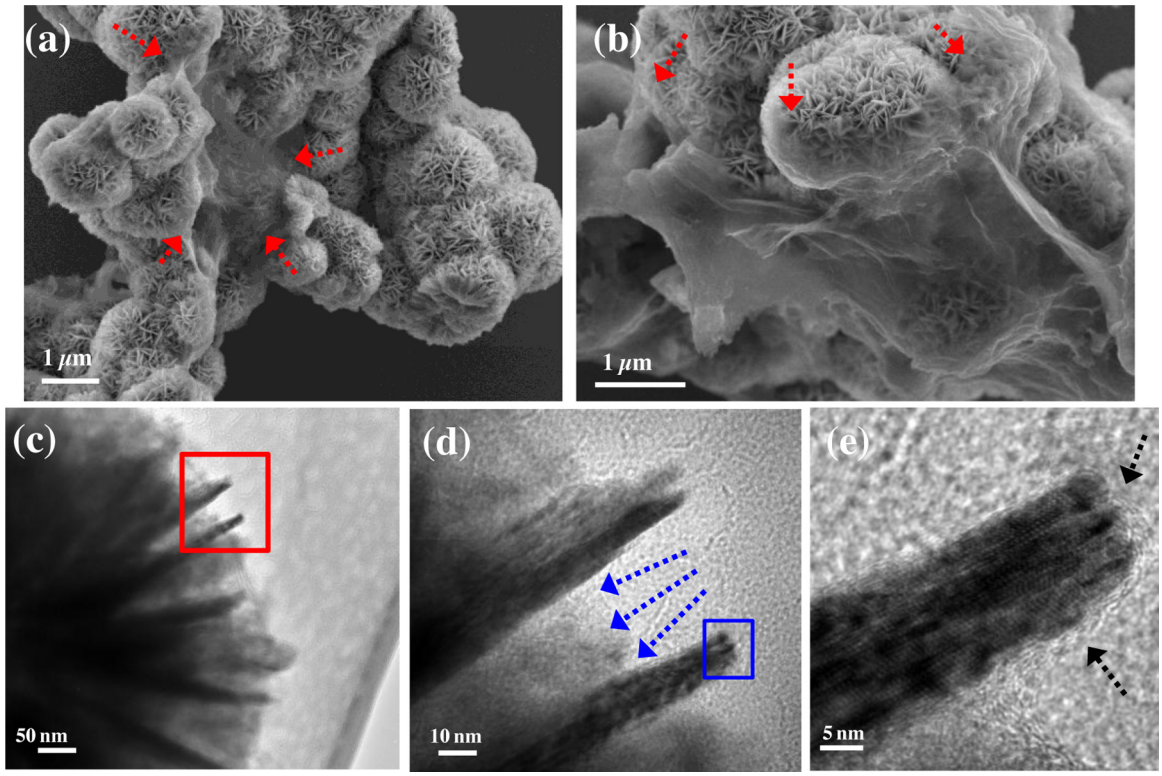

Fig. 5. Graphene hybridized CMO with different graphene contents. (a) The SEM images of **G-0.25-CMO** and (b) **G-0.5-CMO** with the red arrows indicating the graphene coverage boundary. (c) TEM images of **G-0.25-CMO**. (d) The higher magnification TEM images correspond to the red square area in (c). (e) The HR-TEM images correspond to the blue square area in (d). The presence of interfacial graphene hybridization is indicated by the black arrows. (For interpretation of the references to color in this figure legend, the reader is referred to the web version of this article.)

We measured the conductivities and surface areas of graphene hybridized CMO composites (Table 1). As compared to bare CMO, the graphene hybridization significantly increases the surface areas of these composites. **G-CMO** shows the greatest surface area value around 3.5 times higher than CMO. The isotherms of N_2 adsorption–desorption of rGO, CMO, and **G-CMO** are shown in Fig. S-1. The uniform pore sizes (4–6 nm) observed in graphene-based samples (rGO and **G-CMO**) are different from that of bare CMO, demonstrating that the surface porosity features of the hybrids are mainly contributed by graphene. The increase of conductivity due to graphene hybridization was observed as well, where that of **G-CMO** was around one order of magnitude higher than bare CMO. Compared to the conductivity improvement ($\sim 10^3$) caused by structural substitution in cobalt oxides [24], the relatively small increase of conductivity ($\sim 10^1$) is most likely due to the surface wrapping of graphene.

3.2. Electrocatalytic H_2O_2 reduction and sensing

G-CMO composites with superior conductivity and surface areas were tested for electrochemical catalysis and sensing applications. The cyclic voltammetry (CV) results of **G-CMO** show the much stronger characteristic peak of H_2O_2 reduction at −0.48 V than these of rGO and CMO (Fig. 2a). **G-CMO** exhibits the enhanced electrocatalytic activities with the onset potential at around −0.15 V, significantly more positive than these of rGO (−0.25 V), bare CMO (−0.35 V), and the reported metal oxide sensors at ~0.77 V in the literature [35]. In addition, the much stronger peak currents of **G-CMO** are 2.2 and 2.4 times greater than rGO and bare CMO, respectively. These results clearly indicate the synergistic enhancement in electrocatalysis of **G-CMO** due to the effective hybridization of graphene and nanostructured CMO.

The H_2O_2 sensing performance of **G-CMO** was evaluated by measuring the amperometric responses with the successive changes of H_2O_2 concentrations. Fig. 2b shows the typical current-time plot with the systematic increase of H_2O_2 concentrations over time. The rapid, stepwise current changes corresponding to the increase of hydrogen peroxide concentrations were observed (Fig. 2b), showing the H_2O_2 sensing capability of **G-CMO** in a biocompatible condition. The corresponding calibration curves of **G-CMO** (Fig. 2c) show a sensitivity of 11.0 μA/mM ($R^2 = 0.998$), around 2900 and 48 times higher than commercial Co_3O_4 (0.0038 μA/mM) and bare CMO (0.23 μA/mM), respectively. By the continuous sensing operation every day for a week and up to 150 days, **G-CMO**-modified electrodes exhibit the long-term stability under an ambient storage. In this period of time, the measured amperometric responses show a relative standard deviation (RSD) less than 2.9% (Fig. 2d). In addition, the H_2O_2 sensing signals acquired from four different **G-CMO** electrodes showed a RSD of 3.6% (Fig. 2e), indicating the high reproducibility for sensor applications. Fig. 2f demonstrates the sensing selectivity of **G-CMO** with the addition of common interfering species, including dopamine (DA), glucose, ascorbic acid (AA), uric acid (UA), and acetaminophen based on their physiological levels. Negligible signal changes compared to that of H_2O_2 were observed, showing the exceptional anti-interference capability of **G-CMO** than related graphene composites [36]. **G-CMO** clearly manifests the excellent sensitivity, selectivity and stability for biocompatible H_2O_2 detection.

3.3. Graphene/CMO Interfaces

The effect of graphene/CMO interfaces on the synergistic electrocatalysis was investigated by the hybridization

homogeneity and XPS studies. The control samples following the same preparation conditions of **G-CMO** without APTMS modification were prepared and shown in Fig. 3a. These samples that lack the graphene/CMO interface exhibit the more negative onset potentials and weaker magnitude of reduction current as compared to **G-CMO**, indicating no synergistic enhancement between rGO and CMO (Fig. 3b). Thus the formation of graphene/CMO interfaces is critical to achieve the enhanced electrocatalytic activities.

In addition, we compared the XPS results of **G-CMO** with bare CMO, and observed the difference of binding energy (BE) in Co spectra but identical these for Mn species (Fig. 4). The cobalt species hybridized with graphene show the peak shift toward high binding energy region with 0.4 eV and 0.3 eV shifts for Co $2p_{1/2}$ and Co $2p_{3/2}$ respectively, suggesting the increased Co(III) in the mixed-valence pair of Co(II)/Co(III). The greater quantity of Co(III) in the mixed-valence pairs favors the electrocatalytic reduction of H_2O_2 [37]. The higher valence states of Co at the graphene/CMO interfaces may contribute to the greatly enhanced electrocatalysis.

3.4. Effect of 3D nanovoids

To further investigate the role of nanovoids for void-filling behavior of graphene and the enhanced electrocatalysis, two additional samples with decreased contents of graphene were prepared. **G-0.5-CMO** and **G-0.25-CMO**, with one half and one quarter the amount of graphene used in **G-CMO** respectively, show the partial graphene coverage on the nanostructured CMO surface (coverage boundary labeled by red arrows in Fig. 5a and b). With the insufficient amount of graphene, the hybridized graphene tends to distribute locally rather than a homogenous coverage with a relatively thinner thickness on the surface. The TEM results of **G-0.25-CMO** confirm the absence of graphene filling in the nanovoids (more than 80% area), but still show the thin graphene/CMO interfaces (Fig. 5c–e). Such the inhomogeneous distribution may imply that not all the nanovoids of CMO were modified by the APTMS treatment. The initially anchored graphene may induce the further accumulation by π–π stacking until the complete filling in the nanovoids, leading to the local hybridization of graphene.

In the CV comparison of CMO, **G-0.25-CMO**, **G-0.5-CMO**, and **G-CMO** (Fig. 6a), all the graphene hybridized samples exhibit stronger activities of H_2O_2 reduction than bare CMO. Although **G-0.5-CMO** shows the higher reduction currents than **G-0.25-CMO** by ~30%, these two samples display no characteristic reduction peaks as observed in CMO and **G-CMO,** possibly attributed to the different porosities and diffusion kinetics of the two different electrocatalytic sites: bare CMO surface and graphene/CMO interfaces. In addition, **G-0.25-CMO** exhibits the weaker sensitivity (0.71 μA/mM) compared to **G-CMO** (Fig. 2c). These results indicate that the continuous graphene coverage with uniform porosity is critical to achieve rapid mass transport and high electrocatalytic actives.

Based on this observed hybridization behavior, samples that lack the 3D nanovoids should not accumulate the same amount of graphene as **G-CMO** does. To verify this point, we prepared additional CMO that has much smoother surface (less void feature, Fig. 6b), hybridized with the same amount of GO used for **G-CMO**. In the TGA results, this smoother CMO captures the lowered

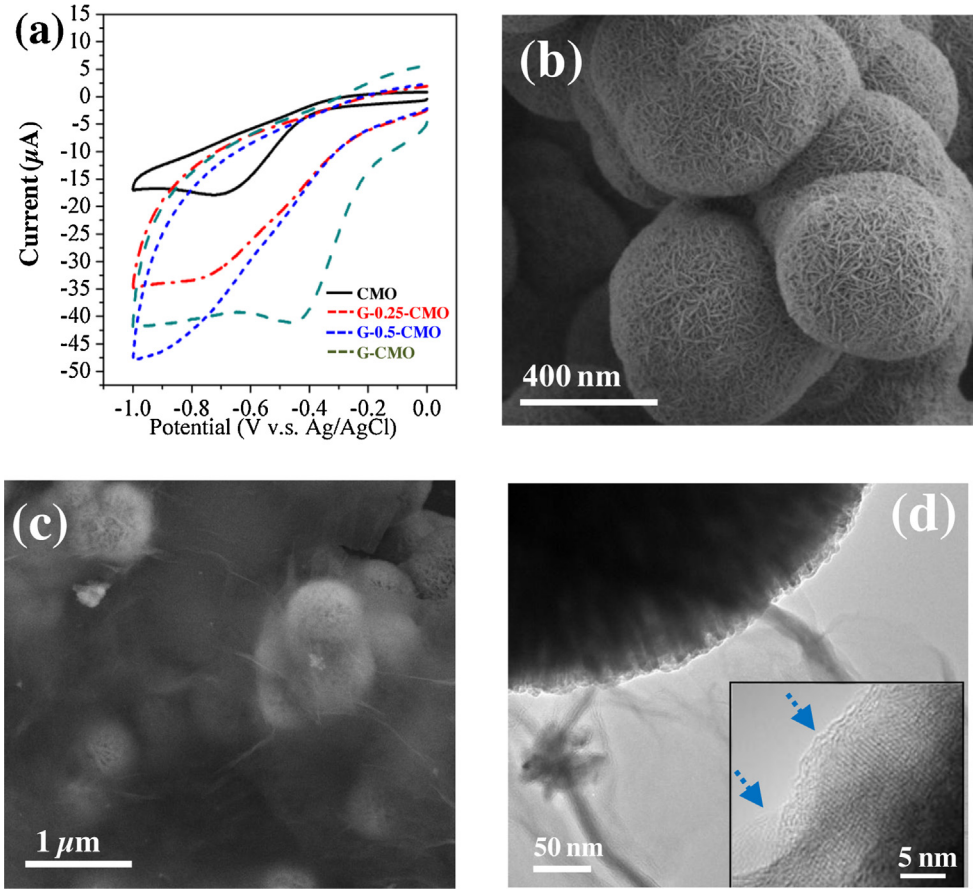

Fig. 6. (a) The comparison of CVs of CMO, **G-0.25-CMO**, **G-0.5-CMO**, and **G-CMO** in the presence of 1 mM H_2O_2 in PBS. (b) The SEM images of the smooth CMO, and (c) its graphene hybrid products. (d) The TEM images of the product in (c). The inset with the higher magnification shows the void-free feature of CMO with the blue arrows indicating the hybridized graphene/CMO interface. (For interpretation of the references to color in this figure legend, the reader is referred to the web version of this article.)

graphene contents decreased by ~25% than **G-CMO**. The electron microscope images in Fig. 6c and d show the even coverage of graphene sheets on the smooth CMO surface without graphene filling observed in **G-CMO**, confirming the presence of nanovoids capable of trapping more graphene for high surface areas.

In addition, the CV results of graphene/smooth CMO composites show the onset potentials for H_2O_2 reduction close to that of G-CMO (around −0.15 V), but with a much weaker reduction current (Fig. S-3). Their comparable onset potentials may support the similar electrocatalytic sites formed at the graphene/CMO interfaces for synergistic electrocatalysis. The weaker reduction currents of graphene/smooth CMO may be attributed to the relatively small graphene contents due to the smooth surface, leading to the smaller surface areas and conductivity for electrocatalysis.

3.5. Graphene coverage and synergistic electrocatalysis

The potential mechanism of electrochemical enhancement in graphene/CMO composites is proposed as illustrated in Scheme 1. The weight percents of graphene content in the composites are nearly proportional to the amounts of graphene used in the preparation (Fig. S-2 and Table 1), yet the drastic enhancement of electrocatalysis only observed in **G-CMO**. Due to the inhomogeneous distribution and graphene on CMO surface, these results imply that a certain amount of graphene is needed to stimulate the synergistic performance. The full graphene coverage in **G-CMO** creates the continuous, conductive charge-transport shells (Scheme 1, right pathway) facilitating the charge-exchange processes at the electrocatalytic interface. The sufficient graphene/CMO hybridization enables **G-CMO** the largest surface areas, smallest onset potentials, greatest reduction currents, as well as the strongest synergistic sensitivity. For **G-0.25-CMO** and **G-0.5-CMO**, the lack of continuous graphene coverage due to the relatively low graphene contents retards the charge transport and hopping process for electrocatalysis (Scheme 1, left pathway). Completed graphene filling in nanovoids may maximize the quantity of graphene/CMO interfaces and surface areas for the optimal graphene-enhanced electrocatalysis. Samples prepared with the higher amount of graphene than **G-CMO** do not exhibit greater electrocatalytic activities (Fig. S-4). Thick graphene coating may block the electrocatalytic-active sites at the interfaces. In addition, the thicker graphene coating could induce a stronger capacity effect, inhibiting the electrocatalytic sensing performance.

4. Conclusion

We demonstrated that **G-CMO** with interfacial combination of pure 2D graphene sheets with 3D nanovoids results in the synergistically enhanced electrocatalysis (2900 and 48 times higher sensitivity than commercial products and bare CMO, respectively). The complexity of nanostructures may govern the trapping amount of graphene and also the composite performance. Controls of the surface modification, graphene coverage, and nanostructures are the effective approaches to manipulate the active interfaces, surface areas, porosities, and conductivity of the as-generated 3D graphene nanocomposites. Combinations between diverse nanostructures and graphene lead to new impacts on the future designs of graphene-hybridized composites, particularly important in upgrading well-developed materials and catalysts.

Acknowledgement

We thank Prof. Jarrn-Horng Lin for the surface area measurement. We acknowledge the funding from Ministry of Science and Technology, Taiwan (R.O.C.) under Grant No. MOST103-2113-M-110-002-MY2, and NSYSU-KMU Joint Research Project NSYSUKMU 103-P015.

Appendix A. Supplementary data

Supplementary data associated with this article can be found, in the online version, at http://dx.doi.org/10.1016/j.electacta.2015.09.041.

References

[1] Y. Liang, H. Wang, J. Zhou, Y. Li, J. Wang, T. Regier, et al., Covalent hybrid of spinel manganese-cobalt oxide and graphene as advanced oxygen reduction electrocatalysts, J. Am. Chem. Soc. 134 (2012) 3517–3523.
[2] C.C. Kuo, C.H. Chen, Graphene thickness-controlled photocatalysis and surface enhanced Raman scattering, Nanoscale 6 (2014) 12805–12813.
[3] I.V. Lightcap, P.V. Kamat, Fortification of CdSe quantum dots with graphene oxide. Excited state interactions and light energy conversion, J. Am. Chem. Soc. 134 (2012) 7109–7116.
[4] K. Parvez, S. Yang, Y. Hernandez, A. Winter, A. Turchanin, X. Feng, et al., Nitrogen-Doped Graphene and Its Iron-Based Composite As Efficient Electrocatalysts for Oxygen Reduction Reaction, ACS Nano 11 (2012) 9541–9550.
[5] J.T. Wang, J.M. Ball, E.M. Barea, A. Abate, J.A. Alexander-Webber, J. Huang, et al., Low-temperature processed electron collection layers of graphene/TiO_2 nanocomposites in thin film perovskite solar cells, Nano Lett. 14 (2014) 724–730.
[6] D. Barpuzary, M. Qureshi, Enhanced photovoltaic performance of semiconductor-sensitized ZnO–CdS coupled with graphene oxide as a novel photoactive material, ACS Appl. Mater. Interfaces 5 (2013) 11673–11682.
[7] R. Kou, Y. Shao, D. Mei, Z. Nie, D. Wang, C. Wang, et al., Stabilization of electrocatalytic metal nanoparticles at metal–metal oxide–graphene triple junction points, J. Am. Chem. Soc. 133 (2011) 2541–2547.
[8] M.S. Sher Shah, A.R. Park, K. Zhang, J.H. Park, P.J. Yoo, Green synthesis of biphasic TiO(2)-reduced graphene oxide nanocomposites with highly enhanced photocatalytic activity, ACS Appl. Mater. Interfaces 4 (2012) 3893–3901.
[9] H. Wang, Y. Yang, Y. Liang, G. Zheng, Y. Li, Y. Cui, et al., Rechargeable Li–O_2 batteries with a covalently coupled $MnCo_2O_4$–graphene hybrid as an oxygen cathode catalyst, Energy Environ. Sci. 5 (2012) 7931.
[10] J. Xu, K. Wang, S.-Z. Zu, B.-H. Han, Z. Wei, Hierarchical Nanocomposites of Polyaniline Nanowire Arrays on Graphene Oxide Sheets with Synergistic Effect for Energy Storage, ACS Nano 9 (2010) 5019–5026.
[11] X. Qi, K.Y. Pu, X. Zhou, H. Li, B. Liu, F. Boey, et al., Conjugated-polyelectrolyte-functionalized reduced graphene oxide with excellent solubility and stability in polar solvents, Small 6 (2010) 663–669.
[12] Z.S. Wu, S. Yang, Y. Sun, K. Parvez, X. Feng, K. Mullen, 3D nitrogen-doped graphene aerogel-supported Fe_3O_4 nanoparticles as efficient electrocatalysts for the oxygen reduction reaction, J. Am. Chem. Soc. 134 (2012) 9082–9085.
[13] B.G. Choi, M.H. Yang, W.H. Hong, J.W. Choi, Y.S. Huh, 3D Macroporous graphene frameworks for supercapacitors with high energy and power densities, ACS Nano 6 (2012) 4020–4028.
[14] R. Wang, C. Xu, J. Sun, L. Gao, H. Yao, Solvothermal-induced 3D macroscopic SnO_2/nitrogen-doped graphene aerogels for high capacity and long-life lithium storage, ACS Appl. Mater. Interfaces 6 (2014) 3427–3436.
[15] W.-N. Li, J. Yuan, X.-F. Shen, S. Gomez-Mower, L.-P. Xu, S. Sithambaram, et al., Hydrothermal synthesis of structure- and shape-controlled manganese oxide octahedral molecular sieve nanomaterials, Adv. Funct. Mater. 16 (2006) 1247–1253.
[16] L.J. Deterding, S. Bhattacharjee, D.C. Ramirez, R.P. Mason, K.B. Tomer, Top-Down and Bottom-Up Mass Spectrometric Characterization of Human Myoglobin-Centered Free Radicals Induced by Oxidative Damage, Anal. Chem. 79 (2007) 6236–6248.
[17] A.M. Nowicka, A. Kowalczyk, S. Sek, Z. Stojek, Oxidation of DNA followed by conformational change after OH radical attack, Anal. Chem. 85 (2013) 355–361.
[18] C. Fonseca, M.A. Barbosa, Corrosion behaviour of titanium in biofluids containing H2O2 studied by electrochgemical impedance spectroscopy, Corros. Sci. 43 (2001) 547–559.
[19] H. Huang, Y.T. Meng, A. Labonte, A. Dobley, S.L. Suib, Large-Scale Synthesis of Silver Manganese Oxide Nanofibers and Their Oxygen Reduction Properties, J. Phys. Chem. C 117 (2013) 25352–25359.
[20] G.C. Van de Bittner, E.A. Dubikovskaya, C.R. Bertozzi, C.J. Chang, In vivo imaging of hydrogen peroxide production in a murine tumor model with a chemoselective bioluminescent reporter, Proc. Natl. Acad. Sci. U S A 107 (2010) 21316–21321.
[21] J. Geng, M. Li, L. Wu, C. Chen, X. Qu, Mesoporous silica nanoparticle-based H_2O_2 responsive controlled-release system used for Alzheimer's disease treatment, Adv. Healthcare Mater. 1 (2012) 332–336.
[22] B. Liu, Z. Sun, P.J. Huang, J. Liu, Hydrogen peroxide displacing DNA from nanoceria: mechanism and detection of glucose in serum, J. Am. Chem. Soc. 137 (2015) 1290–1295.

[23] Y. Cao, R. Yuan, Y. Chai, L. Mao, H. Niu, H. Liu, et al., Ultrasensitive luminol electrochemiluminescence for protein detection based on in situ generated hydrogen peroxide as coreactant with glucose oxidase anchored AuNPs@MWCNTs labeling, Biosens. Bioelectron. 31 (2012) 305–309.
[24] C.C. Kuo, W.J. Lan, C.H. Chen, Redox preparation of mixed-valence cobalt manganese oxide nanostructured materials: highly efficient noble metal-free electrocatalysts for sensing hydrogen peroxide, Nanoscale 6 (2014) 334–341.
[25] W.S. Hummers, R.E. Offeman, Preparation of graphitic oxide, J. Am. Chem. Soc. 80 (1958) 1339.
[26] B. Konkena, S. Vasudevan, Understanding Aqueous Dispersibility of graphene oxide and reduced graphene oxide through pKa measurements, J. Phys. Chem. Lett. 3 (2012) 867–872.
[27] J.S. Lee, K.H. You, C.B. Park, Highly Photoactive, Low Bandgap TiO_2 Nanoparticles Wrapped by Graphene, Adv. Mater. 24 (2012) 1084–1088.
[28] S. Yang, X. Feng, S. Ivanovici, K. Mullen, Fabrication of graphene-encapsulated oxide nanoparticles: towards high-performance anode materials for lithium storage, Angew. Chem., Int. Ed. 49 (2010) 8408–8411.
[29] S. Sreejith, X. Ma, Y. Zhao, Graphene oxide wrapping on squaraine-loaded mesoporous silica nanoparticles for bioimaging, J. Am. Chem. Soc. 134 (2012) 17346–17349.
[30] T. Kurkina, S. Sundaram, R.S. Sundaram, F. Re, M. Masserini, K. Kern, et al., Self-Assembled Electrical Biodetector Based on Reduced Graphene Oxide, ACS Nano 6 (2012) 5514–5520.
[31] W.-J. Lan, C.-C. Kuo, C.-H. Chen, Hierarchical nanostructures with unique Y-shaped interconnection networks in manganese substituted cobalt oxides: the enhancement effect on electrochemical sensing performance, Chem. Commun. 49 (2013) 3025–3027.
[32] Z.-J. Fan, W. Kai, J. Yan, T. Wei, L.-J. Zhi, J. Feng, et al., Facile Synthesis of Graphene Nanosheets via Fe Reduction of Exfoliated Graphite Oxide, ACS Nano 5 (2011) 191–198.
[33] S.S. Srivastava, K. Jain, V.N. Singh, S. Singh, N. Vijayan, N. Dilawar, et al., Faster response of NO_2 sensing in graphene-WO_3 nanocomposites, Nanotechnology 23 (2012) 205501.
[34] O. Akhavan, Graphene Nanomesh by ZnO Nanorod Photocatalysts, ACS Nano 4 (2010) 4174–4180.
[35] H. Pang, F. Gao, Q. Chen, R. Liu, Q. Lu, Dendrite-like Co_3O_4 nanostructure and its applications in sensors, supercapacitors and catalysis, Dalton Trans. 41 (2012) 5862–5868.
[36] W. Huang, Q. Hao, W. Lei, L. Wu, X. Xia, Polypyrrole-hemin-reduce graphene oxide: rapid synthesis and enhanced electrocatalytic activity towards the reduction of hydrogen peroxide, Mater. Res. Express 1 (2014) 045601.
[37] H. Heli, J. Pishahang, Cobalt oxide nanoparticles anchored to multiwalled carbon nanotubes: Synthesis and application for enhanced electrocatalytic reaction and highly sensitive nonenzymatic detection of hydrogen peroxide, Electrochim. Acta 123 (2014) 518–526.